

Near-Field Multipath MIMO Channel Model for Imperfect Surface Reflection

Mohamadreza Delbari¹, George C. Alexandropoulos^{2,3}, Robert Schober⁴, H. Vincent Poor⁵, and Vahid Jamali¹

¹Technical University of Darmstadt, Germany, ²National and Kapodistrian University of Athens, Greece,

³University of Illinois Chicago, USA, ⁴Friedrich-Alexander-Universität Erlangen-Nürnberg, Germany, ⁵Princeton University, USA
e-mails: {mohamadreza.delbari, vahid.jamali}@tu-darmstadt.de, alexandg@di.uoa.gr, robert.schober@fau.de, poor@princeton.edu

Abstract—Near-field (NF) communications is receiving renewed attention in the context of passive reconfigurable intelligent surfaces (RISs) due to their potentially extremely large dimensions. Although line-of-sight (LOS) links are expected to be dominant in NF scenarios, it is not a priori obvious whether or not the impact of non-LOS components can be neglected. Furthermore, despite being weaker than the LOS link, non-LOS links may be required to achieve multiplexing gains in multi-user multiple-input multiple-output (MIMO) scenarios. In this paper, we develop a generalized statistical NF model for RIS-assisted MIMO systems that extends the widely adopted point-scattering model to account for imperfect reflections at large surfaces like walls, ceilings, and the ground. Our simulation results confirm the accuracy of the proposed model and reveal that in various practical scenarios, the impact of non-LOS components is indeed non-negligible, and thus, needs to be carefully taken into consideration.

I. INTRODUCTION

In the field of wireless communication, reconfigurable intelligent surfaces (RISs) have recently gained considerable attention as an enabling technology for realizing programmable radio environments [1, 2]. Comprising sub-wavelength elements, RISs possess the capability to dynamically change the reflected wave facilitating, e.g., the realization of virtual links between base stations (BS) and mobile users (MUs) [3]. For the establishment of a sufficiently large link budget, RISs need to include a substantial number of elements [4]–[6]. Consequently, typical link distances tend to fall into the near-field (NF) regime [7, 8], which makes it imperative to design and analyze RISs for NF communications. Several works have studied RIS-assisted wireless systems in the NF regime; see [9] for a recent tutorial review. For example, assuming an NF line-of-sight (LOS) channel model, the problems of beamforming and localization were studied in [10] and [11], respectively. Moreover, it has been shown in [12] that in the NF regime, data multiplexing is achievable even with LOS links. However, the LOS link may not always be accessible, e.g., due to self-blockage at high frequencies. Thus, also non-LOS links have to be exploited to enhance the multiplexing gain in multi-user multiple-input multiple-output (MIMO) scenarios. Based on a point scattering model, an NF non-LOS channel model was reported in [9, 13]. However, experimental channel measurements suggest that dominant non-LOS components are often caused by large surfaces existing in the environment like walls, ceilings, and the ground, which all have a significant electrical aperture [14,

15]. We henceforth refer to them as non-reconfigurable and non-intelligent surfaces (NSs). These large NSs cannot be modeled by a point scatterer. Furthermore, reflections from NSs may lead to both reflection along the specular direction as well as non-specular directions (i.e., scattering).

To the best of the authors' knowledge, a statistical NF MIMO channel model that accounts for NS has not yet been reported in the literature and is the focus of this work. Our main contributions are summarized as follows.

- We develop a novel NF MIMO channel model, which captures non-LOS paths originating from imperfect reflection by large rough NSs. The model parameters are functions of the variance of roughness variations on the NS, the carrier frequency, the angles of departure (AOD), and the angles of arrival (AOA).
- The non-LOS channel matrix is decomposed into the sum of a deterministic component (i.e., the channel mean) and a stochastic component. By using arguments from geometric optics, we show that regardless of the variance of the NS roughness, the deterministic component always has the form of the channel matrix of an equivalent virtual LOS link caused by an ideal surface reflection (SR). On the other hand, based on the central limit theorem (CLT), we show that the stochastic channel matrix follows a multivariate Gaussian distribution characterized by a covariance matrix. Furthermore, we derive analytical expressions for the covariance matrix for a few special cases. Here, the stochastic component captures the impact of surface scattering (SS).
- We draw various design insights from the proposed model. In particular, we show that the LOS and deterministic non-LOS components of the NF model are functions of real or virtual points in the 3-dimensional space. This observation motivates the need for NF beam focusing for both LOS and NF non-LOS communication.
- Based on a comprehensive set of simulations, we evaluate the accuracy of the proposed channel models in an RIS case study and then verify their statistical parameters. We also demonstrate that non-LOS reflections are necessary to achieve a multiplexing gain in multi-user scenarios.

Notation: Bold capital and small letters are used to denote matrices and vectors, respectively. $(\cdot)^T$, $(\cdot)^H$, and $(\cdot)^*$ denote the transpose, Hermitian, and complex conjugate, respectively. Moreover, $[\mathbf{X}]_{m,n}$ and $[\mathbf{x}]_n$ denote the element in the m th row and n th column of matrix \mathbf{X} and the n th entry of vector \mathbf{x} , respectively. $\mathcal{CN}(\boldsymbol{\mu}, \boldsymbol{\Sigma})$ and $\mathcal{N}(\boldsymbol{\mu}, \boldsymbol{\Sigma})$ denote complex and real Gaussian random vectors with mean vector $\boldsymbol{\mu}$ and covariance matrix $\boldsymbol{\Sigma}$, respectively. $\mathbb{E}\{\cdot\}$ and $\mathbb{V}\{\cdot\}$ represent expectation and variance, respectively, and $\text{Cov}\{\cdot, \cdot\}$ denotes the covariance of two random variables. Finally, $\mathcal{O}(\cdot)$, \mathbb{R} , \mathbb{C} , and $|\mathcal{U}|$ represent the big-O notation, sets of real and complex numbers, and the Lebesgue measure of set \mathcal{U} , respectively.

Delbari and Jamali's work was supported in part by the Deutsche Forschungsgemeinschaft (DFG, German Research Foundation) within the Collaborative Research Center MAKI (SFB 1053, Project-ID 210487104) and in part by the LOEWE initiative (Hesse, Germany) within the emergenCITY center. Alexandropoulos' work was supported by the SNS JU project TERRAMETA under Grant 101097101. Robert Schober's work was funded by the German Ministry for Education and Research (BMBF) under the program of "Souverän. Digital. Vernetzt." joint project 6G-RIC (Project-ID 16KISK023) and the Deutsche Forschungsgemeinschaft (DFG, German Research Foundation) under projects SFB 1483 (Project-ID 442419336, EmpkinS). Poor's work was supported in part by the U.S National Science Foundation under Grants CNS-2128448 and ECCS-2335876.

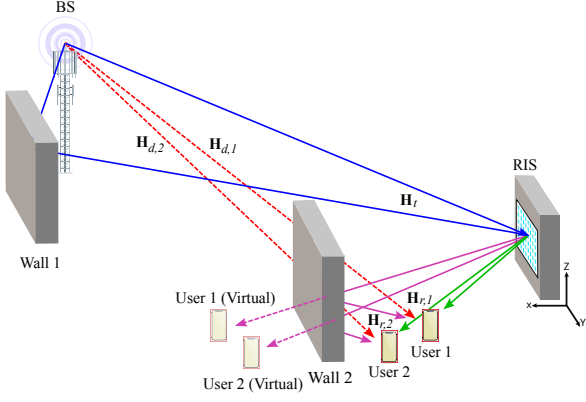


Fig. 1: Schematic illustration of an RIS-assisted downlink K -user wireless communication system when $K = 2$.

II. SYSTEM AND CHANNEL MODELS

In this section, we present our system model and the proposed mixed-scattering NF non-LOS channel model.

A. System Model

We consider a narrow-band downlink communication system that consists of a BS equipped with N_t antennas, an RIS comprising N unit-cells, and K MUs each equipped with N_r antennas, as depicted in Fig. 1. The received signal vector at each k th user ($k = 1, \dots, K$) is given by

$$\mathbf{y}_k = (\mathbf{H}_{d,k} + \mathbf{H}_{r,k} \mathbf{\Omega} \mathbf{H}_t) \mathbf{x} + \mathbf{n}_k, \quad (1)$$

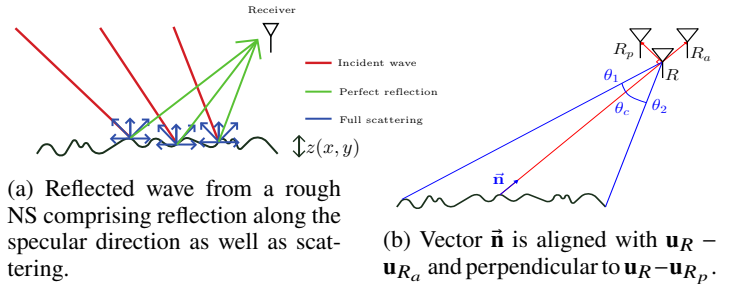
where $\mathbf{x} \in \mathbb{C}^{N_t}$ is the transmit signal vector that satisfies the transmit power constraint $\mathbb{E}\{\|\mathbf{x}\|^2\} \leq P_t$, $\forall k$, with P_t denoting the maximum transmit power. Here, $\mathbf{y}_k \in \mathbb{C}^{N_r}$ and $\mathbf{n}_k \in \mathbb{C}^{N_r}$ represent the received signal vector and the additive white Gaussian noise (AWGN) at the k th MU, respectively, i.e., $\mathbf{n}_k \sim \mathcal{CN}(\mathbf{0}_{N_r}, \sigma_n^2 \mathbf{I}_{N_r})$, $\forall k$, where σ_n^2 is the noise power. Additionally, $\mathbf{\Omega} \in \mathbb{C}^{N \times N}$ is a diagonal matrix with main diagonal entries $\Omega_n e^{j\omega_n}$, where ω_n (with $n = 1, 2, \dots, N$) represents the phase shift applied by each n th RIS unit-cell element and Ω_n is the unit-cell factor. The value of Ω_n depends on wavelength λ , unit-cell area A_{uc} , the AOA, and the AOD [4]. For simplicity, we assume a constant unit-cell factor $\Omega_n = \Omega \triangleq 4\pi A_{uc} \lambda^{-2}$, $\forall n$ [4] (see [16] for a more detailed discussion). Furthermore, $\mathbf{H}_{d,k} \in \mathbb{C}^{N_r \times N_t}$, $\mathbf{H}_t \in \mathbb{C}^{N \times N_t}$, and $\mathbf{H}_{r,k} \in \mathbb{C}^{N_r \times N}$ are the channel matrices for the BS-MU k , BS-RIS, and RIS-MU k links, respectively.

For notational simplicity, in the following, we drop subscripts d , t , r , and k , and specify the channel models for a general matrix $\mathbf{H}_{NF} \in \mathbb{C}^{N_{rx} \times N_{tx}}$ corresponding to N_{tx} transmit antenna elements and N_{rx} receive antenna elements, and wherever necessary, explicitly refer to the BS-MU, BS-RIS, and RIS-MU channels.

B. Existing MIMO NF Channel Model

In the NF regime, the curvature of the wavefront across the receiver (Rx) plane cannot be neglected. Moreover, scatterers in the environment can cause multipath propagation, such that the Rx also receives signals reflected by scatterers via non-LOS paths. The following channel model has been widely used in the literature for the MIMO multipath channel in the NF regime (for example, in [9, Eq. (25)], [13, Eq. (8)], and [17, Eq. (22)]):

$$\mathbf{H}_{NF} = c_0 \mathbf{H}_{NF}^{LOS} + \sum_{s=1}^S c_s \mathbf{H}_s^{scr}, \quad (2)$$



(a) Reflected wave from a rough NS comprising reflection along the specular direction as well as scattering.

(b) Vector \vec{n} is aligned with $\mathbf{u}_R - \mathbf{u}_{R_p}$ and perpendicular to $\mathbf{u}_R - \mathbf{u}_{R_p}$.

Fig. 2: Reflected wave from an NS towards one or several receivers.

where the right-hand-sided channel matrices are defined as follows:

$$[\mathbf{H}_{NF}^{LOS}]_{m,n} = e^{j\kappa \|\mathbf{u}_{rx,m} - \mathbf{u}_{tx,n}\|}, \quad (3)$$

$$\mathbf{H}_s^{scr} = \mathbf{a}_{rx}(\mathbf{u}_s) \mathbf{a}_{tx}^T(\mathbf{u}_s), \quad (4)$$

$$[\mathbf{a}_{tx}(\mathbf{u}_s)]_n = e^{j\kappa \|\mathbf{u}_{tx,n} - \mathbf{u}_s\|}, \text{ and } [\mathbf{a}_{rx}(\mathbf{u}_s)]_m = e^{j\kappa \|\mathbf{u}_{rx,m} - \mathbf{u}_s\|} \quad (5)$$

In (2), without loss of generality, we separate the LOS and non-LOS components of \mathbf{H}_{NF} , respectively, into scalars that determine the power of the channel and normalized matrices that determine the structure of the channel matrix. For example, \mathbf{H}_{NF}^{LOS} is the normalized LOS NF channel matrix and c_0 is the corresponding normalization factor. Here, $\mathbf{u}_{tx,n} = (x_{tx,n}, y_{tx,n}, z_{tx,n})$ and $\mathbf{u}_{rx,m} = (x_{rx,m}, y_{rx,m}, z_{rx,m})$ are the locations of the n th transmitter (Tx) antenna and the m th Rx antenna, respectively, and $\kappa = 2\pi/\lambda$ is the wave number. Moreover, $\mathbf{a}_{tx}(\cdot) \in \mathbb{C}^{N_{tx}}$ and $\mathbf{a}_{rx}(\cdot) \in \mathbb{C}^{N_{rx}}$ denote the Tx and Rx NF array response, respectively, \mathbf{u}_s is the location of the s th scatterer, c_s denotes the normalization factor for the s th non-LOS path, and S is the total number of scatterers. Note that the normalized LOS channel matrix can be written in terms of the Tx and Rx array responses as follows:

$$\mathbf{H}_{NF}^{LOS} = [\mathbf{a}_{rx}(\mathbf{u}_{tx,1}), \dots, \mathbf{a}_{rx}(\mathbf{u}_{tx,N_{tx}})] \quad (6a)$$

$$= [\mathbf{a}_{tx}(\mathbf{u}_{rx,1}), \dots, \mathbf{a}_{tx}(\mathbf{u}_{rx,N_{rx}})]^T. \quad (6b)$$

The non-LOS channel model in (2) is valid under the so-called point scattering assumption which presumes the scattering object is a secondary point source. Due to point scattering, the channel amplitude c_s is proportional to $\frac{1}{\|\mathbf{u}_{rx} - \mathbf{u}_s\| \|\mathbf{u}_s - \mathbf{u}_{tx}\|}$ in this model, where $\mathbf{u}_{tx} = (x_{tx}, y_{tx}, z_{tx})$ and $\mathbf{u}_{rx} = (x_{rx}, y_{rx}, z_{rx})$ are the centers of the transmit and receive arrays, respectively. This observation suggests that unless the scatterer is close to either the Tx or the Rx, the impact of point-source scattering is not significant compared to the LOS link whose channel amplitude c_0 is proportional to $\frac{1}{\|\mathbf{u}_{rx} - \mathbf{u}_{tx}\|}$ [17].

C. Proposed Mixed-Scattering NF non-LOS Channel Model

In practice, the dominant non-LOS components are mainly generated by objects that have significant reflection surfaces (i.e., NS), such as walls, ground, ceiling, etc. [18]. The channel model in (2) is not valid for such scatterers/reflectors. Thus, in this paper, we develop a statistical NF MIMO channel model that accounts for multiple NSs. The proposed channel model has the following form

$$\mathbf{H}_{NF} = c_0 \mathbf{H}_{NF}^{LOS} + \sum_{s=1}^S c_s \mathbf{H}_s^{scr} + \sum_{r=1}^R c_r \mathbf{H}_r^{rf}, \quad (7)$$

where \mathbf{H}_r^{rf} is the normalized non-LOS channel matrix caused by the r th NS in the environment and c_r denotes the corresponding normalization factor. Depending on the operating frequency, the NS can be sufficiently smooth leading to ideal specular reflection, or very rough leading to non-ideal SS. In the following, we focus on modeling of each term $c_r \mathbf{H}_r^{rf}$ in (7).

III. CHANNEL MODEL FOR NON-IDEAL SURFACE REFLECTION

We are interested in characterizing the statistical properties of $c_r \mathbf{H}_r^{\text{rf}}$. To this end, we start by studying the physics behind the reflections from NSs. Then, we decouple $c_r \mathbf{H}_r^{\text{rf}}$ into two main components, namely a deterministic and a stochastic component, and characterize each one separately. Finally, we summarize the proposed model and provide insights for the design of the NF MIMO system, such as beam training and channel estimation schemes.

A. Physics Behind Non-ideal Reflection

Various factors may impact the quality of reflection from an NS. In fact, the surface properties [18], frequency, AOA [14], material losses, and surface roughness [15] may cause scattering, diffraction, and absorption, leading to non-ideal reflection [19]. The key factor determining the relative importance of reflection compared to scattering is the roughness of the surface compared to the wavelength. Therefore, in this section, we start by modeling the surface roughness and analyzing the impact of variations of the roughness over NSs on the non-LOS channel matrix.

1) *Modeling of Roughness:* Assume that the NS (as shown in Fig. 2a) lies in the $x-y$ plane and its height varies in the z direction. Mathematically, one may characterize the height of each point on the NS as a random variable (RV) with a given statistical distribution [20]. We model it as a Gaussian RV and denoted it by Z , as is widely done in the literature [14, 19, 21], i.e., $Z \sim \mathcal{N}(0, \sigma_z^2)$ with σ_z^2 representing the variance of the RV Z .

2) *Impact of Roughness on Reflection:* We adopt the Huygens-Fresnel (HF) principle to evaluate the impact of the NS roughness on reflection. According to this principle, each point along the beam's wavefront is the origin of a secondary spherical wave. Consequently, at any given location, the formation of the new wavefront is the result of the summation of the secondary waves [22, 23]. Thus, each $c_r [\mathbf{H}_r^{\text{rf}}]_{m,n}$ in (7) can be modeled as follows:

$$\frac{E(\mathbf{u}_{\text{rx},m})}{E(\mathbf{u}_{\text{tx},n})} = \frac{\zeta}{j\lambda} \iint_{\mathbf{u} \in \mathcal{U}} \underbrace{\frac{z_{\text{tx},n}}{\|\mathbf{u} - \mathbf{u}_{\text{tx},n}\|^2} \frac{z_{\text{rx},m}}{\|\mathbf{u}_{\text{rx},m} - \mathbf{u}\|^2}}_{\text{amplitude variations}} \times \underbrace{e^{j\kappa \|\mathbf{u} - \mathbf{u}_{\text{tx},n}\|} e^{j\kappa \|\mathbf{u}_{\text{rx},m} - \mathbf{u}\|}}_{\text{phase variations}} dA, \quad (8)$$

where ζ is a constant ensuring surface passivity and accounting for potential losses, $\mathbf{u} = (x, y, z)$ is an arbitrary point on the NS where the center of the NS is located in $(0,0,0)$, dA is the area element, and $E(\mathbf{u}_{\text{rx},m})$ and $E(\mathbf{u}_{\text{tx},n})$ are the electrical fields at the m th Rx and the n th Tx antennas, respectively. Moreover, set \mathcal{U} comprises the total NS area. While (8) accurately models the impact of reflection, solving it for a given realization of $z(x, y)$ over the NS does not lead to a tractable model for system design and cannot provide insights. Throughout the rest of this paper, we refer to (8) as the HF integral, and in Section IV-A, we numerically evaluate it for several scenarios to verify the accuracy of the proposed analytical model.

B. Proposed MIMO NF Channel Model

We first decompose the channel matrix $c_r \mathbf{H}_r^{\text{rf}}$ into the following two components:

$$c_r \mathbf{H}_r^{\text{rf}} = c_{d,r} \mathbf{H}_r^d + c_{n,r} \mathbf{H}_r^n, \quad (9)$$

where the first term is the channel mean and thus deterministic:

$$c_{d,r} \mathbf{H}_r^d \triangleq \mathbb{E}\{c_r \mathbf{H}_r^{\text{rf}}\}, \quad (10)$$

while $c_{n,r} \mathbf{H}_r^n$ captures the channel variations and is hence stochastic. In the following, we characterize the deterministic and stochastic components of $c_r \mathbf{H}_r^{\text{rf}}$ separately.

1) *Deterministic Component:* We henceforth employ different approximations for the area element, amplitude, and phase terms in (8), which are commonly used in the literature to solve complicated HF integral equations [22].

Area Element Approximation: First, let us consider an ideally smooth surface, i.e., $\sigma_z = 0$, for which the area element in (8) becomes $dA = dx dy$. As the NS roughness (σ_z) increases, while each point (x, y) on the NS still acts as a secondary source, this introduces a certain phase shift caused by $z(x, y)$. In this case, we can use approximation $dA \approx dx dy$ in (8) and capture the impact of the NS roughness by the phase terms in (8), i.e., $e^{j\kappa \|\mathbf{u} - \mathbf{u}_{\text{tx},n}\|} e^{j\kappa \|\mathbf{u}_{\text{rx},m} - \mathbf{u}\|}$, which are functions of \mathbf{u} or equivalently $z(x, y)$ [21]. This approximation remains valid when $z(x, y)$ is on the order of wavelengths, which is herein¹ the regime of interest.

Amplitude Approximation: Using Taylor series expansion, we have $\frac{1}{\|\mathbf{u} - \mathbf{u}_{\text{tx},n}\|^2} = \frac{1}{u_{\text{tx},n}^2} + o\left(\frac{u_{\text{tx},n}^{\text{max}} + u_{\text{NS}}^{\text{max}}}{u_{\text{tx},n}^2}\right)$, $\forall \mathbf{u} \in \mathcal{U}, \forall n$, where $u_{\text{tx},n} = \|\mathbf{u}_{\text{tx},n}\|$, $u_{\text{tx},n}^{\text{max}}$ and $u_{\text{NS}}^{\text{max}}$ are the maximum dimensions at the Tx and the NS, respectively. So $\frac{1}{\|\mathbf{u} - \mathbf{u}_{\text{tx},n}\|^2} \approx \frac{1}{u_{\text{tx},n}^2}$ holds when $\frac{u_{\text{tx},n}^{\text{max}} + u_{\text{NS}}^{\text{max}}}{u_{\text{tx},n}^2} \ll 1$. Similarly, we have $\frac{1}{\|\mathbf{u} - \mathbf{u}_{\text{rx},m}\|^2} \approx \frac{1}{u_{\text{rx},m}^2}$, where $u_{\text{rx},m} = \|\mathbf{u}_{\text{rx},m}\|$. Hence,

$$c_r [\mathbf{H}_r^{\text{rf}}]_{m,n} = c_r \iint_{\mathbf{u} \in \mathcal{U}} I(\mathbf{u}, \mathbf{u}_{\text{tx},n}, \mathbf{u}_{\text{rx},m}) dx dy, \quad (11)$$

where $I(\mathbf{u}, \mathbf{u}_{\text{tx},n}, \mathbf{u}_{\text{rx},m}) \triangleq e^{j\kappa \|\mathbf{u} - \mathbf{u}_{\text{tx},n}\|} e^{j\kappa \|\mathbf{u}_{\text{rx},m} - \mathbf{u}\|}$ and $c_r \triangleq \frac{\zeta_r z_{\text{tx},n} z_{\text{rx},m}}{j\lambda u_{\text{tx},n}^2 u_{\text{rx},m}^2}$.

Phase Approximation: The impact of the roughness of the NS affects the phase $\varphi(\mathbf{u}) \triangleq \kappa(\|\mathbf{u}_{\text{tx},n} - \mathbf{u}\| + \|\mathbf{u}_{\text{rx},m} - \mathbf{u}\|)$ according to (11). This term can be simplified as follows, $\varphi(\mathbf{u})$

$$\begin{aligned} &= \kappa \left(u_{\text{tx},n} \sqrt{1 - 2 \frac{\mathbf{u}_{\text{tx},n} \cdot \mathbf{u}}{u_{\text{tx},n}^2} + \frac{\|\mathbf{u}\|^2}{u_{\text{tx},n}^2}} + u_{\text{rx},m} \sqrt{1 - 2 \frac{\mathbf{u}_{\text{rx},m} \cdot \mathbf{u}}{u_{\text{rx},m}^2} + \frac{\|\mathbf{u}\|^2}{u_{\text{rx},m}^2}} \right) \\ &= \kappa \left(u_{\text{tx},n} \sqrt{1 - 2 \frac{x_{\text{tx},n}x + y_{\text{tx},n}y + z_{\text{tx},n}z}{u_{\text{tx},n}^2} + \frac{\|\mathbf{u}\|^2}{u_{\text{tx},n}^2}} \right. \\ &\quad \left. + u_{\text{rx},m} \sqrt{1 - 2 \frac{x_{\text{rx},m}x + y_{\text{rx},m}y + z_{\text{rx},m}z}{u_{\text{rx},m}^2} + \frac{\|\mathbf{u}\|^2}{u_{\text{rx},m}^2}} \right) \end{aligned}$$

$$\stackrel{(a)}{=} \kappa(u_{\text{tx},n} + u_{\text{rx},m} + z \cos(\theta_{\text{tx}}) + z \cos(\theta_{\text{rx}}) + \tilde{f}(x, y, u_{\text{tx},n}, u_{\text{rx},m})) + \mathcal{O}(z^2), \quad (12)$$

where $\cos(\theta_{\text{tx}}) \approx \frac{z_{\text{tx}}}{u_{\text{tx}}}$ and $\cos(\theta_{\text{rx}}) \approx \frac{z_{\text{rx}}}{u_{\text{rx}}}$. Equality (a) follows from a Taylor series expansion and the fact that $\frac{z}{u_{\text{tx},n}}$ and $\frac{z}{u_{\text{rx},m}}$ are typically small, resulting in $\frac{z}{u_{\text{tx},n}} \rightarrow 0$ and $\frac{z}{u_{\text{rx},m}} \rightarrow 0$. Here, \tilde{f} comprises all components that are independent of z . We now calculate the expected value of $c_r [\mathbf{H}_r^{\text{rf}}]_{m,n}$ in (11) with respect to (w.r.t.) the RV Z [21], and obtain the following expression using (10):

$$\begin{aligned} c_{d,r} [\mathbf{H}_r^d]_{m,n} &= \mathbb{E}\{c_r [\mathbf{H}_r^{\text{rf}}]_{m,n}\} \approx c_r \\ &\times \iint_{\mathbf{u} \in \mathcal{U}} \mathbb{E}\{e^{j\kappa z(\cos(\theta_{\text{tx}}) + \cos(\theta_{\text{rx}}))}\} \times \underbrace{e^{j\kappa(u_{\text{tx},n} + u_{\text{rx},m} + \tilde{f})}}_{\text{Deterministic and unaffected by } z} dx dy. \end{aligned} \quad (13)$$

Proposition 1: Assume an NS that is extremely large compared to the Rx/Tx aperture, which is a valid assumption for typical

¹We note that this approximation is not valid for arbitrary surface geometries when $z(x, y) \gg \lambda$.

reflections from walls, ground, ceiling, etc. Moreover, assume that the RV Z follows a Gaussian distribution. Based on these two assumptions, we obtain the expressions:

$$c_{d,r}(g) = \frac{\zeta_r}{j\lambda} \frac{e^{-\frac{g}{2}}}{\|\mathbf{u}_{\text{vtx},n}^r - \mathbf{u}_{\text{tx}}\|} = \frac{\zeta_r}{j\lambda} \frac{e^{-\frac{g}{2}}}{\|\mathbf{u}_{\text{rx}} - \mathbf{u}_{\text{vtx}}^r\|} \quad (14a)$$

$$[\mathbf{H}_r^d]_{m,n} = e^{j\kappa\|\mathbf{u}_{\text{vtx},m}^r - \mathbf{u}_{\text{vtx},n}^r\|} = e^{j\kappa\|\mathbf{u}_{\text{rx},m} - \mathbf{u}_{\text{vtx},n}^r\|}, \quad (14b)$$

where $\mathbf{u}_{\text{vtx},n}^r$ and $\mathbf{u}_{\text{vtx},m}^r$ denote the virtual images of the Tx and Rx mirrored on the r th NS, $\mathbf{u}_{\text{vtx}}^r$ and $\mathbf{u}_{\text{vtx}}^r$ are the centers of the mirror images of the Tx and Rx arrays, respectively (see Fig. 1), and

$$g = \left(\kappa\sigma_z (\cos(\theta_{\text{tx}}) + \cos(\theta_{\text{rx}})) \right)^2. \quad (15)$$

Proof: First, we calculate the expectation of e^{jza} over the Gaussian RV Z with a being a constant. $\mathbb{E}\{e^{jza}\}$ equals to:

$$\begin{aligned} & \int_{-\infty}^{\infty} e^{jza} \frac{1}{\sqrt{2\pi\sigma_z^2}} e^{-\frac{z^2}{2\sigma_z^2}} dz = e^{-\frac{\sigma_z^2 a^2}{2}} \\ & \times \underbrace{\int_{-\infty}^{\infty} \frac{1}{\sqrt{2\pi\sigma_z^2}} e^{-\left(\frac{z}{\sqrt{2}\sigma_z} - j\frac{\sqrt{2}\sigma_z a}{2}\right)^2} dz}_{=1} = e^{-\frac{\sigma_z^2 a^2}{2}}. \end{aligned}$$

By replacing a with $\kappa(\cos(\theta_{\text{tx}}) + \cos(\theta_{\text{rx}}))$, (13) simplifies to:

$$c_{d,r}[\mathbf{H}_r^d]_{m,n} = e^{-\frac{g}{2}} c_r \iint_{\mathbf{u} \in \mathcal{U}} e^{j\kappa(u_{\text{tx},n} + u_{\text{rx},m} + \tilde{r})} dx dy, \quad (16)$$

where the integral term is not a function of z and assumes the same value as for perfect reflection, i.e., $z(x, y) = 0, \forall x, y \in \mathcal{U}$. Hence, $[\mathbf{H}_r^d]_{m,n}$ can be obtained as in (14) using the image theory and geometric optics [24]. ■

Proposition 1 shows that the mean of $c_r \mathbf{H}_r^{\text{fl}}$ always assumes the form of specular reflection, however, its amplitude $c_{d,r}(g)$ decreases as the NS becomes rougher, i.e., σ_z increases. The result in Proposition 1 will be verified for practically large NSs in Section IV-A against the HF integral in (8).

2) *Stochastic Component:* Unlike the point scattering channel model provided in (2), the channel matrix corresponding to a rough NS is not fully deterministic. We derive a statistical model for the NF channel in the following.

Joint PDF of the Elements in \mathbf{H}_r^n in (9): $\varphi(\mathbf{u})$ in (12) has a certain distribution which is identical for all $\mathbf{u} \in \mathcal{U}$. Hence, the probability density function (PDF) of the channel response in (8) can be interpreted as the summation of a large number of RVs with identical distribution, which by CLT [25] leads to a Gaussian distribution for the elements of \mathbf{H}_r^n . This result will be verified in Section IV-A. For a Gaussian distribution, the first and second-order moments are sufficient for a full statistical characterization. Since the mean of \mathbf{H}_r^n is zero by our definition, we analyze the covariance matrix in the following.

Covariance Matrix: The element of the covariance matrix corresponding to the channel coefficients $c_r[\mathbf{H}_r^{\text{fl}}]_{n,m}$ and $c_r[\mathbf{H}_r^{\text{fl}}]_{n',m'}$ is denoted by $\text{Cov}\{c_r[\mathbf{H}_r^{\text{fl}}]_{n,m}, c_r^*[\mathbf{H}_r^{\text{fl}}]_{n',m'}^*\}$. Based on Proposition 1 and using the notation $\alpha_{n,m} \triangleq c_{d,r}(g)[\mathbf{H}_r^d]_{n,m}$ for brevity, yields:

$$\begin{aligned} & \text{Cov}\{c_r[\mathbf{H}_r^{\text{fl}}]_{n,m}, c_r^*[\mathbf{H}_r^{\text{fl}}]_{n',m'}^*\} \\ & = \mathbb{E}\{(c_r[\mathbf{H}_r^{\text{fl}}]_{n,m} - \alpha_{n,m})(c_r[\mathbf{H}_r^{\text{fl}}]_{n',m'} - \alpha_{n',m'})^*\} \\ & \stackrel{(a)}{=} \mathbb{E}\left\{|c_r|^2 \iint_{\mathbf{u} \in \mathcal{U}} I(\mathbf{u}, \mathbf{u}_{\text{tx},n}, \mathbf{u}_{\text{rx},m}) dx dy \iint_{\mathbf{u}' \in \mathcal{U}} I^*(\mathbf{u}', \mathbf{u}_{\text{tx},n'}, \mathbf{u}_{\text{rx},m'}) dx' dy'\right\} \\ & \quad - |c_{d,r}(g)|^2, \end{aligned} \quad (17)$$

where (a) follows from (11) and (14b). In general, (17) cannot be simplified more unless further assumptions are made. We first define three regimes for the surface roughness, σ_z , as follows:

Regime 1: $\kappa\sigma_z \ll 1$: In this case, the NS is sufficiently smooth leading to perfect SR.

Regime 2: This is a transient regime between Regimes 1 and 3, where both surface reflection and scattering are present.

Regime 3: $\kappa\sigma_z \gg 1$: In this case, the NS scatters the wave in all directions leading to full SS.

In Regime 1, the channel is deterministic and readily obtained from Proposition 1. For Regime 2, the HF integral in (8) does not lend itself to an analytical solution and must be solved numerically. However, in Regime 3, we can obtain $|c_{d,r}(g \rightarrow +\infty)|^2 \rightarrow 0$. Without loss of generality, we characterize the normalized covariance denoted as $[\mathbf{R}]_{(n,m,n',m')} \triangleq \frac{1}{|c_r|^2 |\mathcal{U}|} \text{Cov}\{c_r[\mathbf{H}_r^{\text{fl}}]_{n,m}, c_r^*[\mathbf{H}_r^{\text{fl}}]_{n',m'}^*\}$ and refer to it as spatial correlation [26]. We further assume that:

- A1. $\frac{2\|\mathbf{u}_{\text{tx},n} - \mathbf{u}_{\text{tx},n'}\|^2}{\lambda} < u_{\text{tx}}$ and $\frac{2\|\mathbf{u}_{\text{rx},m} - \mathbf{u}_{\text{rx},m'}\|^2}{\lambda} < u_{\text{rx}}$ hold.
A2. $\kappa\|\mathbf{u}_{\text{tx},n} - \mathbf{u}_{\text{tx},n'}\|\sigma_z \ll u_{\text{tx}}$ and $\kappa\|\mathbf{u}_{\text{rx},m} - \mathbf{u}_{\text{rx},m'}\|\sigma_z \ll u_{\text{rx}}$ hold.

Note that A1 and A2 are valid in practice since the distance between nearby antennas with significant correlation is typically much smaller than the Tx-Rx distances. For ease of presentation, let us consider a local spherical coordinate system at the Rx, whose z-axis passes through receive antenna locations $\mathbf{u}_{\text{rx},m}$ and $\mathbf{u}_{\text{rx},m'}$, and whose origin is located at $\frac{\mathbf{u}_{\text{rx},m} + \mathbf{u}_{\text{rx},m'}}{2}$. A similar local coordinate system is defined at the Tx w.r.t. transmit antenna locations $\mathbf{u}_{\text{tx},m}$ and $\mathbf{u}_{\text{tx},m'}$. Based on these assumptions and notations, we obtain the following lemma.

Lemma 1: By assuming Regime 3 under assumptions A1 and A2, (17) can be simplified as follows:

$$\begin{aligned} & [\mathbf{R}]_{(n,m,n',m')} \quad (18) \\ & = \frac{1}{|\mathcal{U}|} \iint_{\mathbf{u} \in \mathcal{U}} e^{j\kappa(\|\mathbf{u}_{\text{rx},m} - \mathbf{u}_{\text{rx},m'}\| \sin(\theta_{\text{rx}}^l(\mathbf{u})) + \|\mathbf{u}_{\text{tx},n} - \mathbf{u}_{\text{tx},n'}\| \sin(\theta_{\text{tx}}^l(\mathbf{u})))} dx dy, \end{aligned}$$

where $\theta_{\text{rx}}^l(\mathbf{u})$ and $\theta_{\text{tx}}^l(\mathbf{u})$ are the elevation angles of point \mathbf{u} evaluated in the Rx and Tx local coordinate systems, respectively.

Proof: The proof is provided in the Appendix. ■

To derive some insights from Lemma 1, let us focus on one Tx antenna and calculate the spatial correlation among two Rx antennas located at $\mathbf{u}_{\text{rx},m}$ and $\mathbf{u}_{\text{rx},m'}$, denoted by $[\mathbf{R}]_{m,m'}$ (note that due to reciprocity, the channel from one Rx antenna to two Tx antennas follows a similar correlation). We assume that the elevation angles $\theta(\mathbf{u}) \forall \mathbf{u} \in \mathcal{U}$ of the points on the NS evaluated in the local Rx spherical coordinate system take value in the interval $[\theta_1, \theta_2]$; see Fig. 2b for an illustration.

Proposition 2: Assuming isotropic scattering within $\theta_1 < \theta(\mathbf{u}) < \theta_2$, the elements of spatial correlation matrix \mathbf{R} are given by

$$|[\mathbf{R}]_{m,m'}| = \text{sinc}\left(\frac{2d_{m,m'}}{\lambda} \cos\left(\frac{\theta_2 + \theta_1}{2}\right) \sin\left(\frac{\theta_2 - \theta_1}{2}\right)\right), \quad (19)$$

where $d_{m,m'} = \|\mathbf{u}_{\text{rx},m} - \mathbf{u}_{\text{rx},m'}\|$ and $\text{sinc}(x) = \frac{\sin(\pi x)}{\pi x}$.

Proof: First, we substitute $\mathbf{u}_{\text{tx},n} = \mathbf{u}_{\text{tx},n'}$ in Lemma 1 and omit indices rx and l for simplicity. Transforming the integral in (18) from Cartesian coordinates into spherical coordinates (i.e., $dx dy = \cos(\theta)d\theta d\phi$), we obtain the expression:

$$[\mathbf{R}]_{m,m'} = \frac{1}{|\mathcal{U}|} \iint_{(\phi, \theta) \in (\Phi, \Theta)} e^{j\kappa\|\mathbf{u}_m - \mathbf{u}_{m'}\| \sin(\theta)} \cos(\theta) d\theta d\phi, \quad (20)$$

where $(\Phi, \Theta) = \{(\phi, \theta) : \phi_1 \leq \phi \leq \phi_2, \theta_1 \leq \theta \leq \theta_2\}$. By substituting $|\mathbf{U}| = (\phi_2 - \phi_1)(\sin(\theta_2) - \sin(\theta_1))$ and continuing the integral calculation, the following result is obtained:

$$\begin{aligned} |[R]_{m,m'}| &= \left| \int_{\phi_1}^{\phi_2} \int_{\theta_1}^{\theta_2} \frac{e^{j\frac{2\pi}{\lambda} \|\mathbf{u}_{m'} - \mathbf{u}_m\| \sin(\theta)}}{(\phi_2 - \phi_1)(\sin(\theta_2) - \sin(\theta_1))} \cos(\theta) d\theta d\phi \right| \\ &= \left| e^{j\frac{\sin(\theta_1) + \sin(\theta_2)}{2} \frac{2\pi}{\lambda} \|\mathbf{u}_{m'} - \mathbf{u}_m\| \frac{\sin(\theta_2) - \sin(\theta_1)}{2}} \frac{\sin\left(\frac{2\pi}{\lambda} \|\mathbf{u}_{m'} - \mathbf{u}_m\| \frac{\sin(\theta_2) - \sin(\theta_1)}{2}\right)}{\frac{2\pi}{\lambda} \|\mathbf{u}_{m'} - \mathbf{u}_m\| \frac{\sin(\theta_2) - \sin(\theta_1)}{2}} \right| \quad (21) \\ &= \text{sinc}\left(\frac{2d}{\lambda} \cos\left(\frac{\theta_2 + \theta_1}{2}\right) \sin\left(\frac{\theta_2 - \theta_1}{2}\right)\right). \end{aligned}$$

This completes the proof. \blacksquare

Proposition 2 reveals that the correlation is maximum (minimum) if $\mathbf{u}_m - \mathbf{u}_{m'}$ is parallel (perpendicular) to $\hat{\mathbf{n}}$ which is the vector pointing from the center of the NS towards the center of the Rx, see R_a and R_p in Fig. 2b. Therefore, we simplify (19) for these two special cases in the following corollary.

Corollary 1: From Proposition 2, we have:

$$|[R]_{m,m'}| = \begin{cases} \text{sinc}\left(\frac{2\|\mathbf{u}_R - \mathbf{u}_{R_a}\|}{\lambda} \sin^2\left(\frac{\theta_c}{2}\right)\right), \theta_1 = -\frac{\pi}{2}, \theta_2 = -\frac{\pi}{2} + \theta_c, \\ \text{sinc}\left(\frac{2\|\mathbf{u}_R - \mathbf{u}_{R_p}\|}{\lambda} \sin\left(\frac{\theta_c}{2}\right)\right), \theta_1 = -\frac{\theta_c}{2}, \theta_2 = \frac{\theta_c}{2}, \end{cases}$$

where we have defined $\theta_c \triangleq \theta_2 - \theta_1$.

Proof: The proof is omitted here due to the space limitation but can be obtained by substituting θ_1 and θ_2 with their definitions and using further trigonometric manipulations. \blacksquare

Corollary 1 offers the following insights. Firstly, as $\sin^2(x) < \sin(x)$, $\forall x \in (0, \pi)$, the correlation between aligned antennas ($\mathbf{u}_m - \mathbf{u}_{m'}$ parallel to $\hat{\mathbf{n}}$) is larger compared to the perpendicular case ($\mathbf{u}_m - \mathbf{u}_{m'}$ perpendicular to $\hat{\mathbf{n}}$) when $\|\mathbf{u}_R - \mathbf{u}_{R_a}\| = \|\mathbf{u}_R - \mathbf{u}_{R_p}\|$. Secondly, increasing the range of the AOA (θ_c) reduces the correlation between antennas. This occurs when the NS is larger or the antennas are closer to the NS. The accuracy of the results in the Corollary 1 will be verified in Section IV-A.

Channel Power Gain: Based on Proposition 1, we can directly calculate the channel power gain in Regime 1 since the channel is deterministic. In Regime 3, the channel power gain can be derived analytically using the law of conservation of energy and exploiting the symmetry of full scattering. In fact, in this regime, the deterministic component is zero, e.g., $e^{-\frac{g}{2}} \rightarrow 0$ in (14), and we argue that the reflected channel power gain is distributed in all directions equally without any preference due to homogeneous SS. We define the channel power gain reflected from the r th NS as $c_{n,r,+\infty}$, which can be derived as follows

$$|c_{n,r,+\infty}|^2 \triangleq \frac{P_{\text{rx}}}{P_{\text{tx}}} = \frac{\zeta_r}{\lambda} \left(\frac{A_{\text{rx}} D_r}{4\pi u_{\text{tx}}^2} \right) \left(\frac{A_r D_{\text{tx}}}{4\pi u_{\text{tx}}^2} \right), \quad (22)$$

where P_{rx} (P_{tx}) is the received power (transmitted power), A_{rx} (A_r) is the Rx (r th NS) effective area, and D_{tx} (D_r) is the Tx (r th NS) directivity. We assume $D_r = 2$ (i.e., 3 dB gain) since NS uniformly reflects the wave *only* in half of the space. Unfortunately, for Regime 2, there is no closed-form solution, and instead (8) needs to be solved. Since this task is not analytically tractable, we model the channel power gain of the stochastic component as follows:

$$\mathbb{E}\{|c_{n,r}(g)|^2\} = (1 - e^{-\frac{g}{2}})^2 |c_{n,r,+\infty}|^2, \quad (23)$$

which is consistent with the limiting values of the channel power gain in Regimes 1 ($g = 0$) and 3 ($g \rightarrow +\infty$). We will show via simulations in Fig. 3 that this heuristic power model closely follows the results obtained by numerically solving the HF integral in (8).

C. Summary and Discussion

The proposed overall NF channel model is summarized as follows

$$\begin{aligned} \mathbf{H}_{\text{NF}} = & c_0 \underbrace{\mathbf{H}_{\text{NF}}^{\text{LOS}}(\mathbf{U}_0)}_{\text{deterministic}} + \sum_{s=1}^S c_s \underbrace{\mathbf{H}_s^{\text{scr}}(\mathbf{U}_s)}_{\text{deterministic}} \\ & + \sum_{r=1}^R \left(\underbrace{c_{d,r} \mathbf{H}_r^d(\mathbf{U}_r)}_{\text{deterministic}} + \underbrace{c_{n,r} \mathbf{H}_r^n}_{\text{stochastic}} \right), \quad (24) \end{aligned}$$

where $\mathbf{U}_0 = [\mathbf{u}_{\text{rx}}, \mathbf{u}_{\text{tx}}]$, $\mathbf{U}_s = [\mathbf{u}_{\text{tx}}, \mathbf{u}_{\text{rx}}, \mathbf{u}_s]$, and $\mathbf{U}_r = [\mathbf{u}_{\text{tx}}, \mathbf{u}_{\text{rx}}, \mathbf{u}_{\text{vtx}}^r, \mathbf{u}_{\text{vtx}}^r]$. Interestingly, the generalized MIMO NF channel model in (24) indicates that all channel components are functions of real or virtual locations of Tx and Rx. This has profound implications in practice for efficient NF beam training [9, 12, 13, 17, 27], where essentially the Tx and Rx learn through NF beam training to focus on the points \mathbf{u}_{tx} , \mathbf{u}_{rx} , $\mathbf{u}_{\text{vtx}}^r$, and $\mathbf{u}_{\text{vtx}}^r$ [28]. Once the NF beamformer leading to a sufficiently high channel power gain is found, the end-to-end channel can be estimated by conventional pilot-based estimators [29].

IV. PERFORMANCE EVALUATION

In the following, we first verify the proposed models with simulations obtained by solving the HF integral, and subsequently, consider a scenario where an RIS serves two users via both LOS and non-LOS links.

A. Model Verification

Simulation Setup: We assume there is a 3×3 m² NS located in the $x - y$ plane where $Z \sim \mathcal{N}(0, \sigma_z^2)$. The carrier frequency is 28 GHz (i.e., $\lambda \approx 1.1$ cm), which implies that the far-field of the NS starts from $\frac{2D^2}{\lambda} = 3288$ m, where D is the largest dimension of the NS. Moreover, the Tx is located at $(0, 0, 90)$, and we consider one Rx whose position is specified for each figure respectively. The NS passivity factor $\zeta = 1$ is adopted for all figures.

In the following, we provide various aspects for the verification of our NF MIMO channel model.

Verification of $\mathbb{E}\{c_r \mathbf{H}_r^{\text{fl}}\}$ and $\mathbb{E}\{|c_r|\}$ in Proposition 1 and (23): Fig. 3 shows one realization of $\text{Re}/\text{Im}\{c_r [\mathbf{H}_r^{\text{fl}}]_{m,n}\}$, $|c_r|$ and the average (Avg.) over 100 normalized samples, as obtained by solving the HF integral in (8) numerically and shown with solid lines. In addition, theoretical results are shown based on Proposition 1 and (25) depicted by square marker. Both the HF integral and theoretical results are normalized to $c_{d,r}(0)$. The curve for $\mathbb{E}\{|c_r|\}$ is obtained using (23) as follows:

$$\frac{\mathbb{E}\{|c_r|\}}{c_{d,r}(0)} = \sqrt{e^{-g} + (1 - e^{-\frac{g}{2}})^2 \frac{|c_{n,r,+\infty}|^2}{|c_{d,r}(0)|^2}}. \quad (25)$$

As can be seen from Fig. 3, the averaged results obtained from the HF integral (solid lines) are in perfect agreement with the proposed theoretical results (square markers). The average of both the real and imaginary parts of $\frac{c_r [\mathbf{H}_r^{\text{fl}}]_{m,n}}{c_{d,r}(0)}$ derived from the HF integral in (8) have identical slopes $e^{-\frac{g}{2}}$ derived from $\frac{c_{d,r}(g)}{c_{d,r}(0)}$ in (14a). Moreover, the average of $\frac{|c_r|}{c_{d,r}(0)}$ obtained from the HF integral asymptotically converges to $\frac{|c_{n,r,+\infty}|}{|c_{d,r}(0)|}$ when $\kappa\sigma_z$ is sufficiently large.

Verification of the PDF of the Elements in \mathbf{H}_r^n : Fig. 4 shows the PDF of $\text{Re}/\text{Im}\{c_r [\mathbf{H}_r^{\text{fl}}]_{m,n}\}$ for $\kappa\sigma_z = 0, 0.5, 3$ obtained with the HF integral in (8). The histograms obtained by numerically solving the HF integral in (8) for various realizations of $z(x, y)$ are in perfect

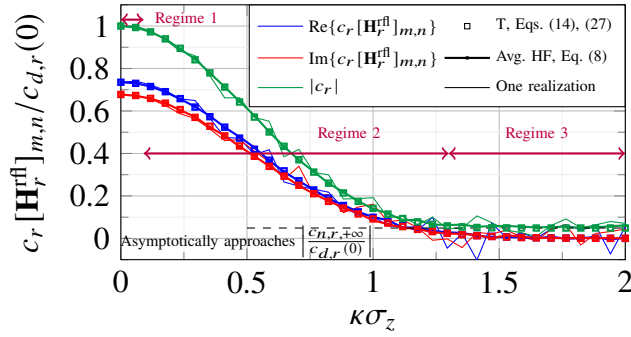


Fig. 3: One realization, average, and theoretical results for the real part, the imaginary part, and the absolute value of the channel amplitude $c_r[\mathbf{H}_r^{\text{rf}}]_{m,n}$ normalized to $c_{d,r}(0)$. Based on the value of $\kappa\sigma_z$, the three different regimes, namely Regime 1 (SR), Regime 2 (transient regime), and Regime 3 (SS), are depicted. Here, T indicates the theoretical result.

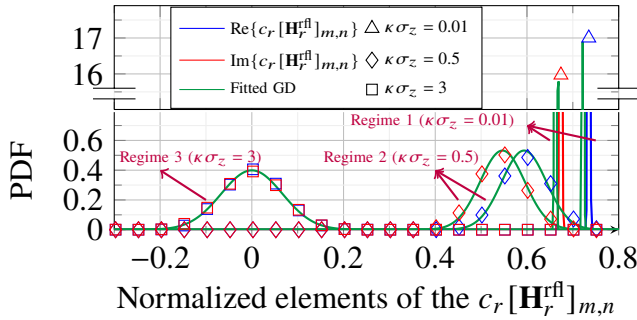


Fig. 4: The distribution of the real and imaginary parts of $c_r[\mathbf{H}_r^{\text{rf}}]_{m,n}$ obtained with the HF integral in (8) normalized by $c_{d,r}(0)$.

agreement with the Gaussian distribution in all three regimes. This validates the adoption of the Gaussian distribution.

Verification of the Correlation of the Elements of \mathbf{H}_r^n in Corollary 1: Figure 5 depicts the spatial correlation between two Rx antennas as a function of their distance. As can be seen, the results of Corollary 1 closely follow the trends of the HF integral approximately. The spatial correlation depends on σ_z , θ_c , and the antennas' positions. We study two particular cases considered in Corollary 1 where $\vec{\mathbf{n}} \perp \mathbf{u}_R - \mathbf{u}_{R_p}$ and $\vec{\mathbf{n}} \parallel \mathbf{u}_R - \mathbf{u}_{R_a}$, respectively, see Fig. 2b. In the first case, the spatial correlation decreases faster with increasing distance than in the second case verifying the results of Corollary 1. Moreover, as Corollary 1 suggests, we observe that the correlation between the antennas increases for smaller θ_c .

B. Impact of Scattering in a Multi-User Scenario

To investigate the impact of NS on NF MIMO communications, we first present the considered setup and benchmark schemes. Subsequently, we present our simulation results.

Simulation Setup: We employ the simulation setup for coverage extension illustrated in Fig. 1. We assume there are $K = 2$ users located at $[23, -23, -5]$ and $[28, -28, -5]$. Moreover, we assume two walls with the following location parameters; wall 1: $x = 45$ m, $30 \text{ m} \leq y \leq 40$ m, $-5 \text{ m} \leq z \leq 5$ m, wall 2: $x = 30$ m, $-27 \text{ m} \leq y \leq -17$ m, $-5 \text{ m} \leq z \leq 5$ m, and we choose ζ to obtain a 3 dB loss for each wall when it reflects in specular direction. The second wall severely blocks the BS-MU channel by -40 dB. The BS comprises a 4×4 uniform planar array (UPA) centered at $[40, 40, 5]$ m parallel to the $x - z$ plane. The RIS comprises

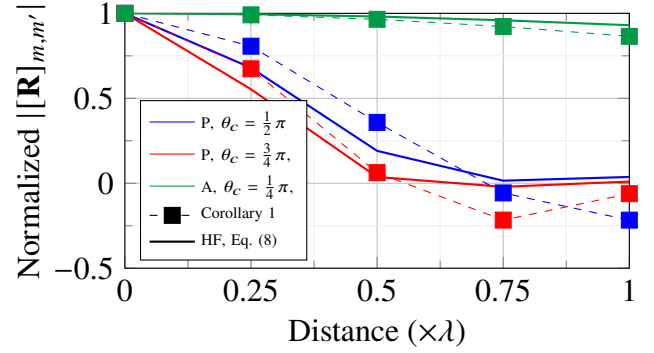


Fig. 5: Comparison of the normalized spatial correlation for different positions of the Rx antennas. For conciseness, we use the abbreviation (P, A), indicating perpendicular and aligned Rx antennas w.r.t. $\vec{\mathbf{n}}$, respectively. For all results, $\kappa\sigma_z = 3$ was used.

a UPA located at $[0, 0, 0]$ m, consisting of $N_y \times N_z$ square tiles along the y - and z -axes, respectively, where $N_y = N_z = 100$. The element spacing for the UPAs at both the BS and RIS is half a wavelength. The MUs have a single antenna ($N_r = 1$). The noise variance is computed as $\sigma_n^2 = WN_0N_f$ with $N_0 = -174$ dBm/Hz, $W = 20$ MHz, and $N_f = 6$ dB. Moreover, the Ricean factor, which is the relative power of the LOS links to the point scattering ones, is set as $K_f = (-100, 100, 8)$ dB for the BS-MU, BS-RIS, and RIS-MU channels, respectively. The center frequency is 28 GHz, the reference path loss at $d_0 = 1$ m is $\beta = -61$ dB, and the path-loss exponent is $\eta = 2$.

Performance Evaluation: Figure 6 shows the achievable sum rate versus (vs.) the BS transmit power for two users. We adopt linear beamforming, where the BS transmits along the LOS and/or the non-LOS BS-RIS channel paths. Similarly, the RIS is divided into 10 tiles, where a given tile reflects the wave along the LOS or the non-LOS RIS-MU channel paths. Moreover, we adopt the algorithm proposed in [30] to optimize the BS and RIS beamformers. To show the benefits of exploiting non-LOS paths for beamforming, we distinguish four cases: *i) (n)LOS-(n)LOS:* The BS and RIS transmit along the LOS and non-LOS paths in both the BS-RIS and RIS-MU channels, respectively. *ii) (n)LOS-LOS:* The RIS reflects the wave only along the LOS RIS-MU paths. *iii) LOS-(n)LOS:* The BS transmits only along the LOS BS-RIS path. *iv) LOS-LOS:* The BS and RIS only exploit the LOS paths for beamforming, which we consider as a benchmark. From Fig. 6, we observe that the performance of the benchmark quickly saturates as the multi-user interference dominates the noise for both users. Moreover, we observe that using the non-LOS paths of only the RIS-MU channels does not improve the performance suggesting that the BS-RIS link is the bottleneck for achieving a multiplexing gain. This observation is confirmed by the performance improvement achieved when the non-LOS BS-RIS path is exploited for beamforming. Here, in the NF regime, the RIS with its large aperture is able to simultaneously focus on both MUs, despite the fact that they are located in the same direction from the RIS. A further gain can be achieved when the non-LOS paths of both the BS-RIS and the RIS-MU channels are exploited for beamforming, which is due to the additional spatial diversity. In summary, Fig. 6 underlines the importance of exploiting the non-LOS components created by NS in multi-user scenarios.

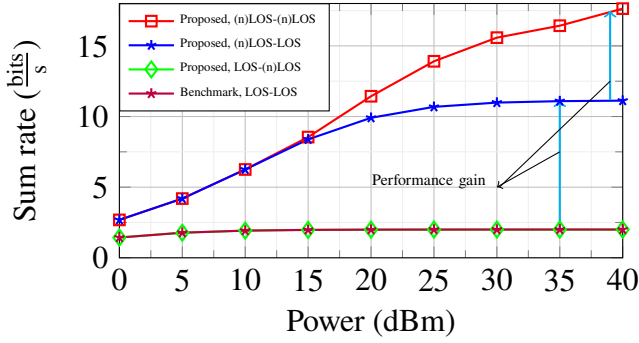


Fig. 6: Sum rate vs. transmit power for $K = 2$.

V. CONCLUSION

In this paper, we have introduced a new NF MIMO channel model accounting for reflections from NSs in addition to the LOS link and point scattering. Although recent measurement campaigns have shown the relevance of imperfect reflection from large NSs in the environment, the existing channel models do not account for this effect, constituting a research gap that is addressed in this paper. We have verified the accuracy of the proposed model by comparing it with the numerical evaluation of the Huygens- Fresnel integral in (8). Furthermore, via simulations, we have demonstrated that the impact of NSs is not only non-negligible but also beneficial for achieving a multiplexing gain in multi-user communication scenarios.

APPENDIX

Consider (17) and decouple it into the following two cases:

Case 1 ($\mathbf{u}' \neq \mathbf{u}$):

$$[\mathbf{R}]_{(n,m,n',m')} = \frac{1}{|\mathcal{U}|} \iint_{\mathbf{u} \in \mathcal{U}} \iint_{\mathbf{u}' \in \mathcal{U}} \mathbb{E} \left\{ I(\mathbf{u}, \mathbf{u}_{\text{Tx},n}, \mathbf{u}_{\text{Rx},m}) \right\} \times \mathbb{E} \left\{ I^*(\mathbf{u}', \mathbf{u}_{\text{Tx},n'}, \mathbf{u}_{\text{Rx},m'}) \right\} d\mathbf{x} d\mathbf{y}' d\mathbf{x} d\mathbf{y}, \quad (26)$$

resulting in $[\mathbf{R}]_{(n,m,n',m')} = 0$ since each expectation inside the double integrals is zero in Regime 3.

Case 2 ($\mathbf{u}' = \mathbf{u}$):

First, let us expand the term of $\|\mathbf{u} - \mathbf{u}_{\text{Rx},m'}\|$ in terms of $\|\mathbf{u} - \mathbf{u}_{\text{Rx},m}\|$. Thereby, $\|\mathbf{u} - \mathbf{u}_{\text{Rx},m'}\|$ is equal to the following quantity:

$$\|\mathbf{u} - \mathbf{u}_{\text{Rx},m}\| + \|\mathbf{u}_{\text{Rx},m} - \mathbf{u}_{\text{Rx},m'}\| \sin(\theta_{\text{Rx}}^l) + \mathcal{O}(\|\mathbf{u}_{\text{Rx},m} - \mathbf{u}_{\text{Rx},m'}\|^2). \quad (27)$$

Note that, based on Assumption A1, we can neglect the last term in (27). A similar expansion can be made for the Tx side by substituting the indices rx and m with tx and n, respectively. To this end, the expression for $[\mathbf{R}]_{(n,m,n',m')}$ simplifies as follows:

$$[\mathbf{R}]_{(n,m,n',m')} = \frac{1}{|\mathcal{U}|} \times \iint_{\mathbf{u} \in \mathcal{U}} \mathbb{E} \left\{ e^{j\mathbf{k} \cdot (\|\mathbf{u}_{\text{Rx},m} - \mathbf{u}_{\text{Rx},m'}\| \sin(\theta_{\text{Rx}}^l) + \|\mathbf{u}_{\text{Tx},n} - \mathbf{u}_{\text{Tx},n'}\| \sin(\theta_{\text{Tx}}^l))} \right\} d\mathbf{x} d\mathbf{y}. \quad (28)$$

Finally, we can omit the expectation based on Assumption A2.

REFERENCES

- [1] M. Di Renzo *et al.*, "Smart radio environments empowered by AI reconfigurable meta-surfaces: An idea whose time has come," *EURASIP J. Wireless Commun. Netw.*, vol. 129, no. 129, pp. 1–20, May 2019.
- [2] X. Yu, V. Jamali, D. Xu, D. W. K. Ng, and R. Schober, "Smart and reconfigurable wireless communications: From IRS modeling to algorithm design," *IEEE Wireless Commun.*, vol. 28, no. 6, pp. 118–125, 2021.
- [3] W. Tang *et al.*, "Wireless communications with reconfigurable intelligent surface: Path loss modeling and experimental measurement," *IEEE Trans. Wireless Commun.*, vol. 20, no. 1, pp. 421–439, 2020.

- [4] M. Najafi, V. Jamali, R. Schober, and H. V. Poor, "Physics-based modeling and scalable optimization of large intelligent reflecting surfaces," *IEEE Trans. Commun.*, vol. 69, no. 4, pp. 2673–2691, 2020.
- [5] E. Björnson and L. Sanguinetti, "Rayleigh fading modeling and channel hardening for reconfigurable intelligent surfaces," *Wireless Commun. Lett.*, vol. 10, no. 4, pp. 830–834, 2020.
- [6] G. C. Alexandropoulos *et al.*, "Reconfigurable intelligent surfaces for THz: Signal processing and hardware design challenges," in *Proc. European Conf. Ant. Prop. (EuCAP)*, Glasgow, Scotland, 2024, pp. 1–5.
- [7] E. Björnson and L. Sanguinetti, "Power scaling laws and near-field behaviors of massive MIMO and intelligent reflecting surfaces," *IEEE Open J. Commun. Soc.*, vol. 1, pp. 1306–1324, 2020.
- [8] T. Gong *et al.*, "Near-field channel modeling for holographic MIMO communications," *IEEE Wireless Commun.*, vol. 31, no. 3, pp. 108–116, 2024.
- [9] Y. Liu *et al.*, "Near-field communications: A tutorial review," *IEEE Open J. of the Commun. Society*, 2023.
- [10] H. Lu and Y. Zeng, "Near-field modeling and performance analysis for multi-user extremely large-scale MIMO communication," *IEEE Commun. Lett.*, vol. 26, no. 2, pp. 277–281, 2021.
- [11] D. Dardari, N. Decarli, A. Guerra, and F. Guidi, "LOS/NLOS near-field localization with a large reconfigurable intelligent surface," *IEEE Trans. Wireless Commun.*, vol. 21, no. 6, pp. 4282–4294, 2021.
- [12] P. Ramezani and E. Björnson, "Near-field beamforming and multiplexing using extremely large aperture arrays," in *Fundamentals of 6G Communications and Networking*. Springer, 2023, pp. 317–349.
- [13] Y. Lu and L. Dai, "Near-field channel estimation in mixed LOS/nLOS environments for extremely large-scale MIMO systems," *IEEE Trans. Commun.*, vol. 71, pp. 3694–3707, 2023.
- [14] C. Jansen *et al.*, "Diffuse scattering from rough surfaces in THz communication channels," *IEEE Trans. THz Science Tech.*, vol. 1, no. 2, pp. 462–472, 2011.
- [15] F. Sheikh *et al.*, "Scattering and roughness analysis of indoor materials at frequencies from 750 GHz to 1.1 THz," *IEEE Trans. Antennas Propag.*, vol. 69, no. 11, pp. 7820–7829, 2021.
- [16] Q. Wu, S. Zhang, B. Zheng, C. You, and R. Zhang, "Intelligent reflecting surface-aided wireless communications: A tutorial," *IEEE Trans. Commun.*, vol. 69, no. 5, pp. 3313–3351, 2021.
- [17] M. Delbari, G. C. Alexandropoulos, R. Schober, and V. Jamali, "Far- versus near-field RIS modeling and beam design," in *Reconfigurable Metasurfaces for Wireless Communications: Architectures, Modeling, and Optimization*. Springer, arXiv preprint: <https://arxiv.org/pdf/2401.08237>, 2023.
- [18] E. N. Grossman, N. Popovic, R. A. Chamberlin, J. Gordon, and D. Novotny, "Submillimeter wavelength scattering from random rough surfaces," *IEEE Trans. Terahertz Sci. Technol.*, vol. 7, no. 5, pp. 546–562, 2017.
- [19] A. M. Khamse, X. Dong, and N. Ferdinand, "The scattering channel model for terahertz wireless communications," *IEEE Open J. Commun. Soc.*, vol. 4, pp. 810–822, 2023.
- [20] M. Alissa, F. Sheikh, A. A.-h. Abbas, and T. Kaiser, "Wave scattering from non-Gaussian rough surfaces at terahertz frequencies," in *Proc. IEEE Int. Workshop Mobile THz Sys. (IWMTS)*, Bad Neuenahr, Germany, 2019, pp. 1–5.
- [21] F. Shi, M. Lowe, and R. Craster, "Recovery of correlation function of internal random rough surfaces from diffusely scattered elastic waves," *J. Mech. Phys. Solids*, vol. 99, pp. 483–494, 2017.
- [22] J. W. Goodman, *Introduction to Fourier Optics*. Roberts and Company publishers, 2005.
- [23] H. Ajam, M. Najafi, V. Jamali, and R. Schober, "Channel modeling for IRS-assisted FSO systems," in *Proc. IEEE Wireless Commun. Netw. Conf. (WCNC)*, 2021, pp. 1–7.
- [24] C. A. Balanis, *Antenna Theory: Analysis and Design*. Hoboken, NJ, USA: Wiley, 2005.
- [25] A. Papoulis, *Probability, Random Variables and Stochastic Processes*. Boston: McGraw-Hill, 2002.
- [26] G. C. Alexandropoulos, N. C. Sagiias, F. I. Lazarakis, and K. Berberidis, "New results for the multivariate Nakagami- m fading model with arbitrary correlation matrix and applications," *IEEE Trans. Wireless Commun.*, vol. 8, no. 1, pp. 245–255, 2009.
- [27] P. Gavrilidis and G. C. Alexandropoulos, "Near-field beam tracking with extremely massive dynamic metasurface antennas," *arXiv preprint arXiv:2406.01488*, 2024.
- [28] G. C. Alexandropoulos, V. Jamali, R. Schober, and H. V. Poor, "Near-field hierarchical beam management for RIS-enabled millimeter wave multi-antenna systems," in *Proc. IEEE Sensor Array and Multichannel Signal Process. Workshop (SAM)*, Trondheim, Norway, 2022, pp. 460–464.
- [29] V. Jamali, G. C. Alexandropoulos, R. Schober, and H. V. Poor, "Low-to-zero-overhead IRS reconfiguration: Decoupling illumination and channel estimation," *IEEE Commun. Lett.*, vol. 26, no. 4, pp. 932–936, 2022.
- [30] V. Jamali, W. Ghanem, R. Schober, and H. V. Poor, "Impact of channel models on performance characterization of RIS-assisted wireless systems," in *Proc. European Conf. Ant. Prop. (EuCAP)*, Florence, Italy, 2023, pp. 1–5.